Effect of processing kinetics on the structure of ferromagnetic-ferroelectric-ferromagnetic interfaces

P. S. Sankara Rama Krishnan, Q. M. Ramasse, Wen-I Liang, Ying-Hao Chu, V. Nagarajan, and P. Munroe

Citation: Journal of Applied Physics **112**, 104102 (2012); doi: 10.1063/1.4765045
View online: http://dx.doi.org/10.1063/1.4765045
View Table of Contents: http://scitation.aip.org/content/aip/journal/jap/112/10?ver=pdfcov
Published by the AIP Publishing

Effect of processing kinetics on the structure of ferromagnetic-ferroelectric-ferromagnetic interfaces

P. S. Sankara Rama Krishnan,[1] Q. M. Ramasse,[2] Wen-I Liang,[3] Ying-Hao Chu,[3] V. Nagarajan,[1] and P. Munroe[1]
[1]*School of Materials Science and Engineering, The University of New South Wales, Sydney NSW2052, Australia*
[2]*SuperSTEM Laboratory, STFC Daresbury Campus, Keckwick Lane, Daresbury WA4 4AD, United Kingdom*
[3]*Department of Materials Science and Engineering, National Chiao Tung University, Taiwan*

(Received 14 May 2012; accepted 12 October 2012; published online 21 November 2012)

Trilayer heterostructures consisting of a ferroelectric bismuth ferrite (BFO) film sandwiched between ferromagnetic lanthanum strontium manganese oxide (LSMO) films were fabricated using pulsed laser deposition. Both BFO thicknesses (20 nm, 5 nm) and cooling rates were varied to investigate the role of processing parameters on the chemistry of the interfaces. The interfaces were investigated using a dedicated aberration corrected scanning transmission electron microscope (STEM) operated at 100 kV via STEM-high angle annular dark field (STEM-HAADF) and STEM-electron energy loss spectroscopy (STEM-EELS) modes. Combined analysis through STEM-HAADF and STEM-EELS revealed the formation of lattice distortion in certain regions of the BFO layer for the ~5 nm film. Piezoresponse force microscopy (PFM) studies of the ~5 nm BFO sample revealed weak ferroelectric domain switching. Stacking fault defects with mixed valence manganese (Mn-B site cation) were formed in the top LSMO layer when the heterostructure was cooled at a slower rate irrespective of BFO thickness, thereby demonstrating the effect of processing kinetics on the physical integrity of the heterostructure. © *2012 American Institute of Physics*. [http://dx.doi.org/10.1063/1.4765045]

I. INTRODUCTION

The introduction of a ferroelectric material as a barrier layer in a tunnel junction device has recently attracted attention.[1,2] In such ferroelectric tunnel junctions (FTJs), magnetic moments of the ferromagnetic electrodes can be reversed by changing the polarization direction of the ferroelectric barrier. The electrical control of such magnetic moments results in additional degrees of freedom which can be explored as novel spintronic devices.[3–6] The performance of FTJs is strongly influenced by interfacial effects between the ferromagnetic-ferroelectric-ferromagnetic (FM/FE/FM) or metal-ferroelectric-metal (ME/FE/ME) interfaces depending on the choice of electrode material. At FE/FM interfaces structural asymmetry is created across the interface.[7] This may result in creation of an electrical dipole even in the paraelectric state, and this can directly influence the stability and function of these tunnel junction devices. The formation of misfit dislocations due to interfacial strain, chemical inhomogeneity at the interfaces, and the work function between FE/FM interfaces[8] are the primary mechanisms that directly influence the functional stability at this interface. A dislocation core may have unit cell dimensions, but the strain field associated with it is long range.[9] Both the electronic states[10] and microstructure[11] of these ferroelectric heterostructures are adversely affected by the presence of such long range strain fields. Stoichiometry is also expected to change at the dislocation core.[12] A non-stoichiometric dislocation core can lead to pinning of ferroelectric domains resulting in the loss of ferroelectric properties. For a superior FTJ device performance, an atomically sharp FM-FE interface[13] without any defects or dislocations is a prerequisite. Therefore, it is instructive to systematically investigate both the role of thin film processing parameters on the interfacial chemistry of such heterostructures and their impact on device functionality.

In this report, the fabrication and atomic level characterization of a ferromagnetic lanthanum strontium manganese oxide ($La_{0.7}Sr_{0.3}MnO_3$) (LSMO) and multiferroic bismuth ferrite ($BiFeO_3$) (BFO) heterostructure are discussed. A LSMO-BFO-LSMO trilayer heterostructure was fabricated under a range of processing conditions using pulsed laser deposition (PLD). In addition to varying the BFO thickness (20 nm, 5 nm), two different quench rates (20 °C min^{-1}, 5 °C min^{-1}) from the deposition temperature were used to fabricate the heterostructure in order to understand the effect of this processing condition on the structural quality of the interfaces.

The LSMO-BFO-LSMO heterostructure interfaces were analysed using a dedicated aberration corrected scanning transmission electron microscope (STEM) operated at 100 kV. The physical nature of the interface was analysed using STEM-high angle annular dark field (STEM-HAADF) imaging. The chemical properties across the interface structures were obtained using STEM-electron energy loss spectroscopy (STEM-EELS). The combined analysis of the STEM-HAADF, STEM-bright field, and STEM-EELS data reveal the formation of lattice distortions in local regions of the ~5 nm thick BFO film. Piezoresponse force microscopy (PFM) studies of the ~5 nm BFO sample revealed weak ferroelectric domain switching in line with size effect trends. Stacking fault (SF) defects containing Mn ions of variable

valence were formed in the top LSMO layer, when the heterostructure was cooled at a slower rate, irrespective of the BFO thickness.

II. EXPERIMENTAL METHODS

A. Trilayer (LSMO-BFO-LSMO) heterostructure fabrication using PLD

The LSMO bottom layer was first deposited on a strontium titanate (STO) (001) substrate at an oxygen partial pressure of 100 mTorr and deposition temperature of 700 °C. A $La_{0.7}Sr_{0.3}MnO_3$ target with a density of 6.1 g cm^{-3} and a purity of 99.99% was used. The laser energy was ~4 to 5 J cm^{-2} with a repetition rate of 10 Hz. The BFO middle layer was then deposited at an oxygen partial pressure of 100 mTorr and 700 °C. Here, BFO, with a 7.3 g cm^{-3} density and 99.99% purity was used as the target. For this layer the laser energy density was ~4 to 5 J cm^{-2} with a repetition rate of 10 Hz. The top LSMO layer was deposited subsequently using the same deposition conditions that were used for the bottom LSMO layer. The STO-LSMO-BFO-LSMO heterostructure was then cooled in an oxygen-rich pressure of 500 Torr.

The acronyms used to identify the prepared specimens are LS—LSMO, BF—BFO, SC—slow cooling, FC—fast cooling and the numerical values give the corresponding film thicknesses. The faster and slower cooling rates were 20 °C min^{-1} and 5 °C min^{-1}, respectively. The BFO thickness values were 5 nm and 20 nm.

In addition, bilayer samples (LSMO-BFO) with two different BFO thicknesses (LS70BF20FC and LS70BF5FC) were prepared on a STO (001) substrate using the same PLD conditions described above and cooled at 20 °C min^{-1}. To perform domain studies of the BFO layer using PFM, the top LSMO electrode is not required.

B. TEM studies

Cross-sectional TEM specimens were prepared using the tripod method followed by conventional ion beam thinning. Bright field TEM images were obtained using a Philips CM 200 field emission gun (FEG) microscope operated at 200 kV. Atomic resolution Z-contrast STEM images were obtained using the dedicated aberration corrected STEM equipped with a cold field emission electron source. Atomic resolution STEM-EELS studies were carried out by acquiring line scans across the LSMO-BFO-LSMO interface in a dedicated STEM (Nion-corrected VG ultra-STEM) operated at 100 kV and equipped with an Enfina parallel EELS detector. The O-K, Fe-$L_{2,3}$, La-$M_{4,5}$, and Mn-$L_{2,3}$ edges were simultaneously acquired, using a dispersion of 0.3 eV per channel. The convergence and collection semi-angles were 21 mrad and 19 mrad, respectively.

C. PFM studies

PFM studies were carried out for samples without the top LSMO layer. Bilayer LSMO-BFO samples were fabricated using the conditions described above, and PFM studies were carried out using a Multimode-Digital Instruments scanning probe microscope. First, a $3 \times 3\ \mu m^2$ area was scanned for topography. A negative bias was applied over an area of $2 \times 2\ \mu m^2$. This was followed by a positive bias over an area of $1\ \mu m^2$. A bias voltage of −/+4 V and −/+2.5 V was used for the 20 nm and 5 nm samples, respectively. To observe the domain switching, a topographic scan was carried out over a $3 \times 3\ \mu m^2$ area after removing the bias. The out-of-plane image is reported.

III. RESULTS AND DISCUSSION

A. LS70BF20LS60FC sample

A STEM-HAADF image of the fast cooled ~20 nm thick BFO sample is shown in Figure 1(a). The thickness of the bottom LSMO film is ~70 nm, whilst the top LSMO film thickness is ~60 nm. The thickness of the BFO layer is ~20 nm. These values are in agreement with those expected from the PLD deposition conditions. Higher resolution images of the bottom LSMO-BFO interface and top LSMO-BFO interface are given in Figures 1(b) and 1(c), respectively. The atomic resolution visible in these STEM-HAADF images reveals that both the bottom and top interfaces are relatively sharp with chemical intermixing limited of the order of ~1.2 nm. No misfit dislocations were observed at either interface. Results from STEM-EELS analysis across both the bottom and top interface are shown in Figures 1(d) and 1(e), respectively. EEL spectra were obtained for O-K, Mn-$L_{2,3}$, Fe-$L_{2,3}$ and La-$M_{4,5}$ edges at energies of 510 eV, 655 eV, 708 eV, and 840 eV, respectively. The survey image indicating the line scan position across the interfaces is shown separately.

The six data points shown in Figure 1(d) were recorded over a distance of 7 nm. On analysis, moving from top to bottom the Mn-$L_{2,3}$ and La-$M_{4,5}$ edges start to become weak between point 3 and point 2, whilst the Fe-$L_{2,3}$ edge starts to appear more strongly at point 2. The Mn-$L_{2,3}$ and La-$M_{4,5}$ edges completely disappear at point 1 (the Fe-$L_{2,3}$ edges become much stronger) and this transition from LSMO to BFO takes place over a distance of ~1.2 nm. In Figure 1(e), moving from top to bottom the Mn-$L_{2,3}$ and La-$M_{4,5}$ edges, start appearing at point 3, whilst the Fe-$L_{2,3}$ edge starts to weaken at point 2. At point 1, only Mn-$L_{2,3}$ and La-$M_{4,5}$ edges were observed with no Fe-$L_{2,3}$ edge. Again, this transition takes place over a distance of ~1.2 nm. Thus, the STEM-EELS line scans across top and bottom interfaces confirm that the chemical intermixing across the top and bottom interfaces is not greater than four unit cells.

It must be highlighted that the spatial resolution of EELS maps or line scans in STEM-EELS is still the subject of ongoing investigations.[14] Effects such as EELS signal delocalisation, dynamical electron beam broadening can play a major role in direct interpretation of EELS data.[15] However, in the present investigation, STEM-HAADF and STEM-EELS data were acquired respectively with a spatial resolution of the order ~0.15 to 0.2 nm and the energy spread of the spectrometer is of the order of 0.3 eV. In addition to collecting experimental data using highly stable conditions to minimize the effect of noise and artefacts, the background noises in the EEL spectra were removed using a principle component

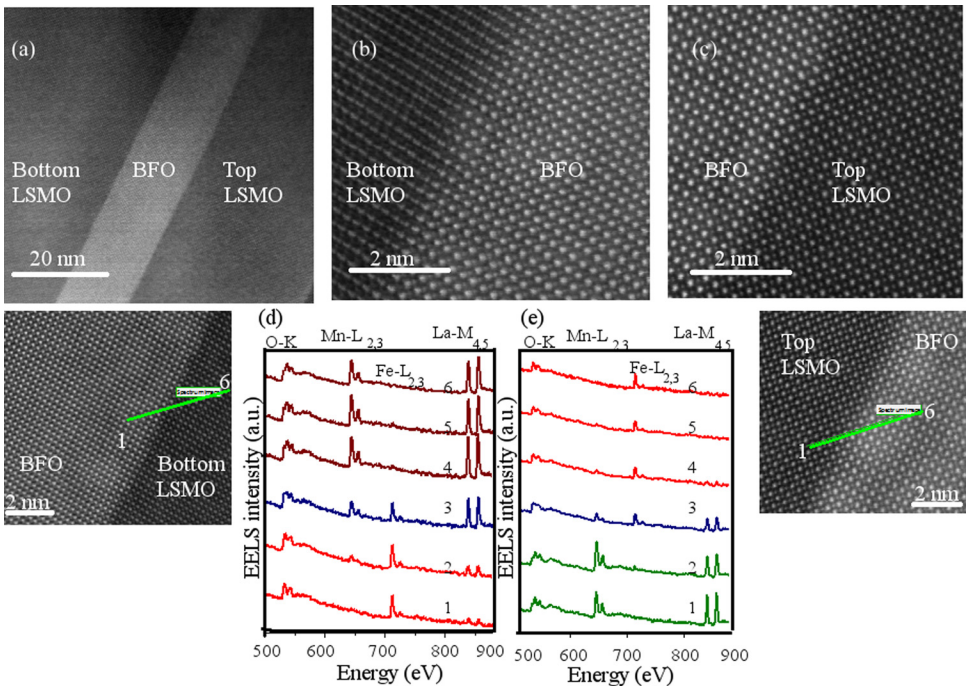

FIG. 1. (a) STEM-HAADF image of LS70BF20LS60FC confirming thickness of each layer. (b) and (c) STEM-HAADF images of LS70BF20LS60FC confirming sharp bottom and top interfaces. (d) STEM-EELS of LS70BF20LS60FC confirming the diffusion across the bottom interface is about three unit cells (~1.2 nm). (e) STEM-EELS of LS70BF20LS60FC confirming the diffusion across the top interface is about three unit cells (~1.2 nm).

analysis (PCA) method.[16] Hence, the observation of four unit cell diffusion across the interfaces is from the sample rather than due to any instrumental artefacts. Hence, it can be concluded that the LSMO-BFO-LSMO heterostructure exhibits relatively sharp interfaces (that is, diffusion not more than a few unit cells) when fabricated using rapid cooling conditions.

B. LS70BF5LS60FC sample

A STEM-HAADF image of the fast cooled ~5 nm BFO sample is shown in Figure 2(a). The low resolution image confirms the thickness of each layer as being close to the nominally expected value. Images of both the top and bottom interfaces are shown in Figure 2(b) and again clearly reveal that the interfaces are epitaxial and free of dislocations. The STEM-EELS data from both the bottom and top interfaces are shown in Figures 2(c) and 2(d), respectively. EEL spectra were obtained for O-K, Mn-$L_{2,3}$, Fe-$L_{2,3}$, and La-$M_{4,5}$ edges at energies of 510 eV, 655 eV, 708 eV, and 840 eV, respectively. The survey image indicating the line scan position across the interfaces is also shown. On analysis, moving from top to bottom, there is measurable intensity of the

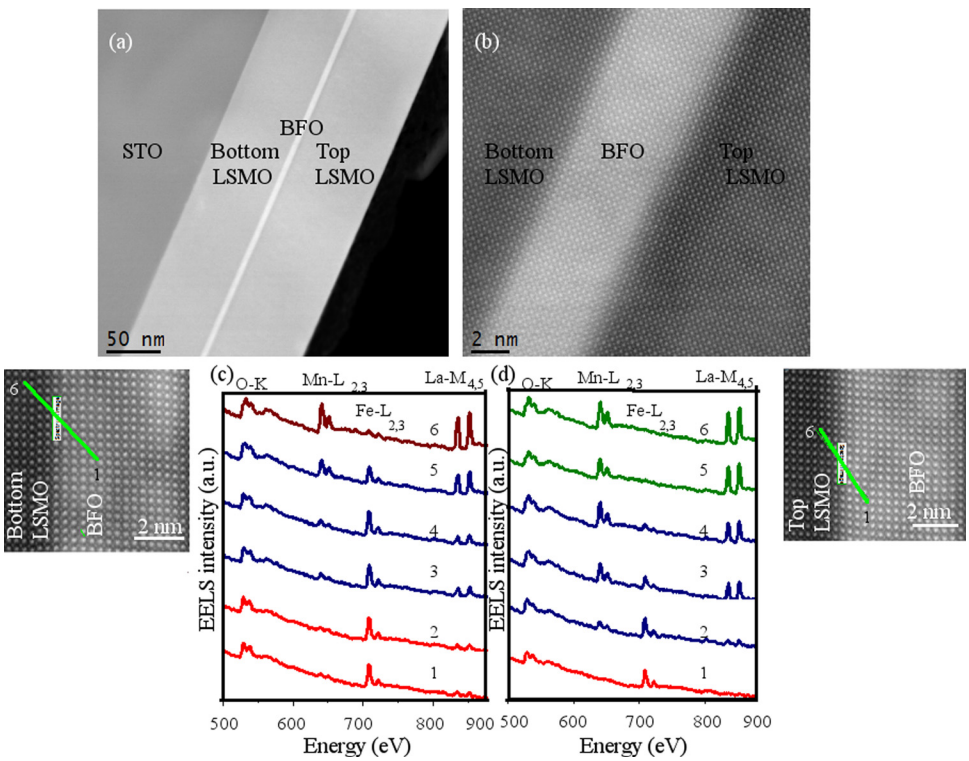

FIG. 2. (a) STEM-HAADF image of LS70BF5LS60FC confirming the thickness. (b) STEM-HAADF image of LS70BF5LS60FC confirming the defect-free top and bottom interfaces. (c) STEM-EELS data of LS70BF5LS60FC bottom interface showing diffusion across interface over a distance of ~2 nm. (d) STEM-EELS data of LS70BF5LS60FC top interface showing diffusion across the interface over a distance of ~1.5 nm.

Fe-$L_{2,3}$ edge even before the complete disappearance of the Mn-$L_{2,3}$ and La-$M_{4,5}$ edges (reference points 3 to 5). This edge completely disappears at reference point 1. This result confirms that there is an intermixing of elements at the bottom interface over a length scale of ~2.8 nm (~8 unit cells).

Similarly, the spectra across top LSMO and the BFO interface are shown in Figure 2(d). On analysis, moving from top to bottom, there is measurable Mn-$L_{2,3}$ and La-$M_{4,5}$ edges along with the Fe-$L_{2,3}$ peak (point 2). At point 1, only Fe-$L_{2,3}$ edge is observed. This overlap takes place over a distance of ~1.5 nm, which is clearly larger than the instrument resolution. Thus, the STEM-EELS line scan across both top and bottom interfaces confirms that Fe, Mn, and La diffuse across both interfaces by 1.5 to 2.5 nm. This is in contrast with the sample with the larger BFO thickness, where, chemically the interfaces were sharper with a diffusion of elements is about half the distance measured here. This is surprising as intuitively one would expect the thicker films (that are exposed at higher temperatures for longer times) to show any diffusion.

A STEM-bright field image of LS70BF5LS60FC is shown in Figure 3. It can be observed that at some regions in the BFO, the lattice appears to be disrupted. For example, the atomic column intensity profile defined by the blue rectangle (inset) in the BFO layer shows a non-uniform variation, consistent with the possible presence of defects in localised regions.

The observation of increased chemical diffusion across the LSMO-BFO interfaces and the lattice distortion in the BFO layer in this sample may be related to the decrease in BFO thickness. The epitaxial strain at the interfaces due to lattice parameter differences between LSMO and BFO for the 20 nm specimen (LS70BF20LS60FC) may be gradually relaxed because of the increased thickness. However, in the 5 nm sample (LS70BF5LS60FC), the BFO layer thickness may be too small to completely accommodate the non-negligible lattice mismatch (~2.2%) between these layers, and this promotes an epitaxial-strain induced chemical diffusion across the interface. During BFO thin film fabrication defects such as oxygen vacancies, the reduction of Fe^{3+} to Fe^{2+} and the formation of secondary phases like α, γ–Fe_2O_3 have been observed and have been attributed due to variations in oxygen pressure during film processing and changes in BFO film thickness levels.[17–19] In addition to this, BFO thin films below a critical thickness of ~20 nm are fully strained.[20] These heteroepitaxial strains have been shown to induce structural modifications.[21] During fabrication of the LS70BF5LS60FC sample, there was no variation in oxygen pressure, thereby the likelihood for defects due to oxygen deficiency is eliminated. In the STEM-bright field image (Figure 3), the BFO film is continuous without any segregation or isolated particle formation. This confirms that there is no separate secondary phase formation in the BFO film. The observed higher interfacial diffusion (more than 8 unit cells) across the LSMO-BFO interfaces and the formation of a distorted BFO lattice in this low BFO thickness sample can be attributed to the uncompensated epitaxial strains between the different constituents of the heterostructure. Further, by keeping the processing conditions unchanged and varying only the thickness of the BFO layer, the chemical homogeneity and the structural integrity of the LSMO-BFO-LSMO heterostructure appeared to be compromised.

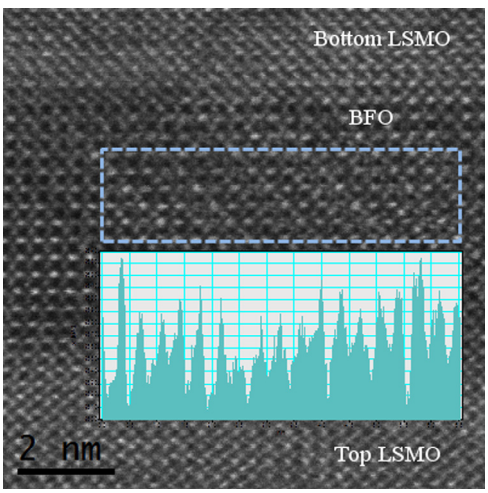

FIG. 3. STEM-bright field image of LS70BF5LS60FC showing the lattice distortions and the inset shows a non-uniform image intensity profile (a.u).

C. PFM studies

In order to understand the effect of variations in BFO thickness, as well as the presence of defective structures on the ferroelectric properties of BFO, PFM studies were carried out. The PFM data for LS70BF20FC and LS70BF5FC are shown in Figures 4(a) and 4(c), respectively. For the LS70BF20FC sample, Figures 4(a) and 4(b) represent the topography and out-of-plane images, respectively.

The PFM data for the LS70BF20FC sample show domain switching at a write voltage of ±4 V. Figures 4(c) and

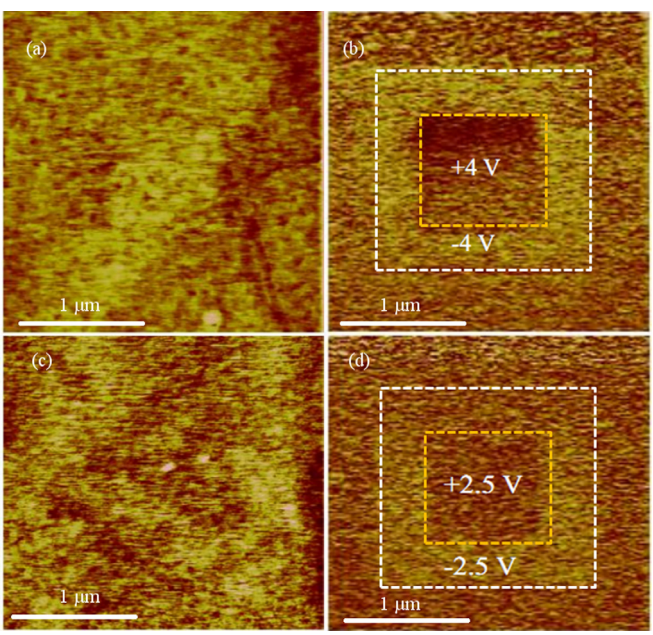

FIG. 4. (a) and (b) Topography and out-of-plane image of LS70BF20FC, respectively. The out-of-plane image shows a ferroelectric switching at −/+ 4 V. (c) and (d) topography and out-of-plane image of LS70BF5FC, respectively. The out-of-plane image shows a ferroelectric switching at −/+ 2.5 V.

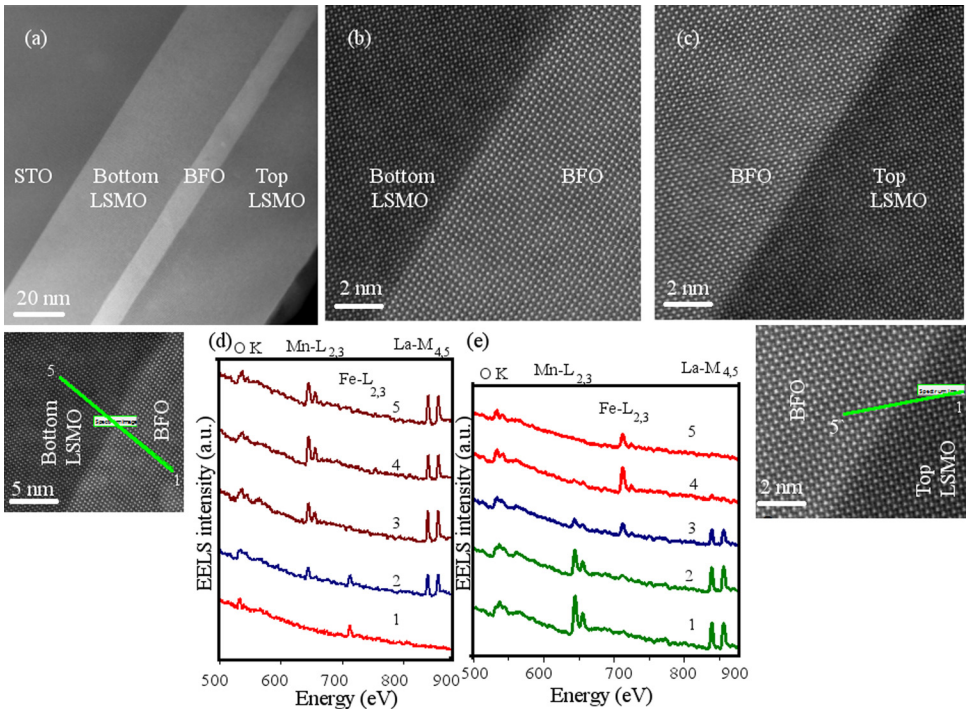

FIG. 5. (a) STEM-HAADF image the SC sample confirming each layer thickness. (b) and (c) STEM-HAADF images of bottom and top interface, respectively showing dislocation-free interfaces. (d) and (e) STEM-EELS across bottom and top interfaces, respectively, revealing chemical diffusion of about one unit cell.

4(d) show the topography and out-of-plane images of the LS70BF5FC sample, respectively. The PFM images of the LS70BF5FC show only a weak domain switching at ±2.5 V. The write voltage is reduced for this sample due to the reduced (~5 nm) BFO thickness. The PFM studies indicate in the LS70BF5FC sample, despite the combination of factors such as ultra-low thin film thickness (~5 nm), diffused interfaces and the presence of locally defective regions, that the BFO is still able to exhibit ferroelectric domain switching.

D. SC sample

In order to study the effect of change in processing kinetics on the quality of the interfaces, a LSMO-BFO-LSMO heterostructure with the thick BFO was cooled at a very slow rate (5 °C min^{-1}). A low resolution image of the SC structure is shown in Figure 5(a). This again confirms that the thickness of each layer is close to the expected values. STEM-HAADF images are shown in Figures 5(b) and 5(c), respectively, for the bottom and top interfaces. These show that both interfaces are epitaxial and free of misfit dislocations. Linescans were recorded across both interfaces. The STEM-EELS data for both the bottom and top interfaces are given in Figures 5(d) and 5(e), respectively. EEL spectra were obtained for O-K, Mn-$L_{2,3}$, Fe-$L_{2,3}$ and La-$M_{4,5}$ edges at energies of 510 eV, 655 eV, 708 eV, and 840 eV, respectively. Analysis of the Mn-$L_{2,3}$, La-$M_{4,5}$, and Fe-$L_{2,3}$ profiles do not reveal a gradual chemical intermixing at both bottom and top interfaces, thereby implying that both the interfaces are chemically sharp, within the resolution limits of the instrument used, which is of the order of ~0.15 to 0.2 nm.

However, the STEM-HAADF images (Figures 6(a) and 6(b)) of the top LSMO layer reveal the presence of stacking faults originating ~7 nm from the top BFO-LSMO interface. The stacking faults are observed at regular intervals of ~10 to 12 nm from each other in the top LSMO layer. In addition to this, it can be observed that in the [001] direction an additional plane of atoms is present every half a unit cell (Figure 6(b)). The length of each stacking fault defect is ~1.6 nm. The appearance of extra plane of atoms is repeated in the [100] direction every three unit cells (~1 nm).

EEL spectra obtained for Mn-$L_{2,3}$ and La-$M_{4,5}$ edges across the stacking fault region and the adjacent area are shown in Figures 7(b) and 7(c), respectively. Figure 7(a) shows a region at the top LSMO layer containing a stacking fault were EELS analysis was performed. The STEM-EELS line scan was carried out from point 1 to point 12 and the position of spectra 8 closely matches the stacking fault region. From Figure 7(b), it can be observed that at EEL spectra number 8 for the Mn edge, a peak-like feature appears at energy of 640 eV and is not seen in the spectra above (up to spectrum 12) or below (down to spectrum 1). This confirms that there is a change in the chemical composition in the stacking fault region, whilst in the adjacent unfaulted region no similar chemical variation is observed. The

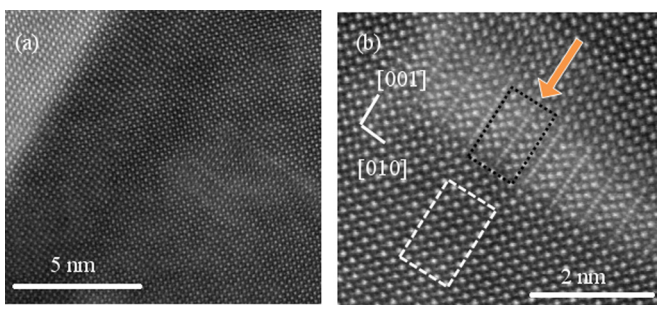

FIG. 6. (a) and (b) STEM-HAADF images of SC sample revealing the presence of stacking fault at the top LSMO. The stacking fault at the top LSMO layer appears at ~7 nm from the top BFO-LSMO interface. The arrow in (b) indicate the appearance of extra atomic plane in the [001] direction. The white box indicates a defect-free region adjacent to stacking fault.

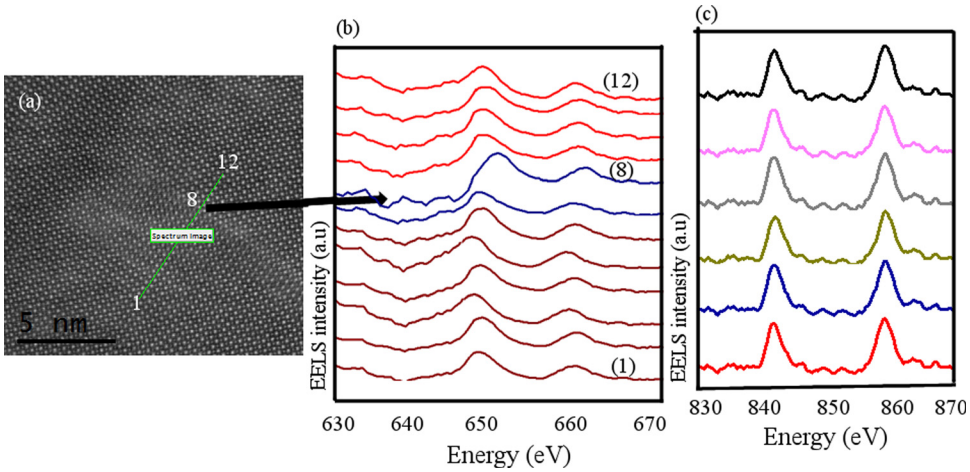

FIG. 7. (a) STEM-EEL spectrum image of the SC sample showing the EELS acquisition points across the stacking fault and adjacent regions. (b) EEL Spectra of Mn-$L_{2,3}$ edge shows appearance of peak-like feature at 640 eV at the staking fault (spectrum number 8). The peak is not observed in the adjacent regions of the stacking fault (spectrum 1 or spectrum 12). (c) La-$M_{4,5}$ edge spectra without any additional feature confirming the no change in La valence state.

peak at 640 eV for the Mn-$L_{2,3}$ edge corresponds to a valence state of Mn^{2+}.[22–24] Thus, the Mn within the stacking fault consists of a mixed valence state comprising Mn^{2+} and Mn^{3+}. Conversely, from the Figure 7(c), it can be observed that the La-$M_{4,5}$ edge show no such changes, confirming no change in La valence in the faulted region. In thin film heterostructures, segregation of LSMO into non-stoichiometric composition with the formation of compounds such as MnO (compounds with reduced Mn (Mn^{2+}) valence) is a commonly observed defect mechanism. These types of defects are observed when the heterostructure is annealed at high temperature (~450 °C) under vacuum conditions[25–27] and exhibit a deleterious effect on the magnetic properties and the magnitude of spin polarization of LSMO.[22,28,29]

In the SC sample, the formation of stacking faults and the associated change in chemical signature of Mn can be related to the kinetics of heterostructure fabrication. When the cooling rate is reduced from 20 °C min^{-1} to 5 °C min^{-1} the duration of high temperature exposure (temperatures greater than ~450 °C) of the heterostructure is increased from ~90 min to ~240 min. Thus, it appears that the extended duration at high temperatures is sufficient to induce segregation of LSMO resulting in the change in the Mn valence. This leads to the formation of stacking faults at a distance ~7 nm from the top interface. In addition to this, there is no formation of dislocations at the interface hence defect formation due to misfit dislocations can be excluded. In heteroepitaxial films below a critical thickness, the misfit strain due to lattice mismatch is elastically accommodated by the formation of coherent interfaces.[30] In perovskite oxide heterostructures with a mismatch of ~2.5% to 3%, above the critical thickness formation of misfit dislocation is favoured.[31] Defects such as threading dislocations (TDs), SFs, and creation of chemical inhomogeneity across the interfaces can also be formed as an alternate mechanism for reliving the accumulated strains associated with the heterostructure formation, depending upon the energetically favoured conditions.[32,33] When such dislocations are formed the strain field around the dislocation core disturbs the lattice periodicity. As a major finding in this study, for the STO-LSMO-BFO heterostructure with a mismatch of ~2.2%, the extended duration (90 min against 240 min) at higher temperatures provides sufficient thermal energy for segregation and mobility of chemical constituents for the top LSMO layer. Thus, the physical integrity of the heterostructure is disturbed by the formation of stacking faults and creation of chemical inhomogeneity at the top LSMO. The formation of these defects becomes a favoured mechanism to accommodate the effect of kinetic energy associated with high temperature, rather than formation of misfit dislocation at the top interface. By contrast, similar defects were not observed in the faster cooled samples. Although lattice distortion is observed at the reduced BFO thickness, there were no stacking faults present in this heterostructure. Finally, the significance of heterostructure fabrication on the physical and chemical integrity of LSMO-BFO-LSMO interfaces is established clearly.

IV. SUMMARY AND CONCLUSIONS

In summary, ferromagnetic-ferroelectric-ferromagnetic (LSMO-BFO-LSMO) heterostructures were fabricated using PLD and were structurally and chemically characterized using dedicated aberration corrected STEM. Three different specimens were fabricated, in two specimens the ferroelectric thickness (LS70BF20LS60FC, and LS70BF5LS60FC) was varied, while in the third specimen the cooling condition from the fabrication temperature (SC) was varied. The 20 nm BFO thickness specimen exhibited relatively sharp top and bottom interfaces with chemical intermixing limited to the order of ~1.2 nm, while the 5 nm BFO thickness samples showed top and bottom interfaces with diffusion of cations across both interfaces over a length scale of ~2.5 nm. Lattice distortions were observed in the 5 nm BFO specimen. PFM studies confirmed a very weak ferroelectric switching in the ~5 nm BFO film thereby confirming that the presence of lattice distortion is a localised phenomenon. Stacking fault defects associated with local variations in Mn valence were formed on the top LSMO layer when the samples were cooled slowly. This was attributed to the increased cation mobility due to the extended time the specimen was exposed to high temperatures. It is observed that fabrication conditions play a significant role in determining the structural quality of the heterostructure interfaces.

ACKNOWLEDGMENTS

P.S.S. thanks Adam Sikorski (ACMM, University of Sydney) for assistance provided during the cross sectional

specimen preparation. This work at The University of New South Wales was supported by an ARC Discovery project (DP0771432). The authors acknowledge access to the UNSW node of the Australian Microscopy & Microanalysis Research Facility (AMMRF). Part of this work was carried out at the SuperSTEM Laboratory,funded by Engineering and Physical Research Council (EPSRC), U.K.

[1]V. Garcia, S. Fusil, K. Bouzehouane, S. Enouz-Vedrenne, N. D. Mathur, A. Barthelemy, and M. Bibes, Nature **460**, 81 (2009).
[2]V. Garcia, M. Bibes, L. Bocher, S. Valencia, F. Kronast, A. Crassous, X. Moya, S. Enouz-Vedrenne, A. Gloter, D. Imhoff, C. Deranlot, N. D. Mathur, S. Fusil, K. Bouzehouane, and A. Barthélémy, Science **327**, 1106 (2010).
[3]F. Yang, M. H. Tang, Z. Ye, Y. C. Zhou, X. J. Zheng, J. X. Tang, J. J. Zhang, and J. He, J. Appl. Phys. **102**, 044504 (2007).
[4]J. P. Velev, C.-G. Duan, J. D. Burton, A. Smogunov, M. K. Niranjan, E. Tosatti, S. S. Jaswal, and E. Y. Tsymbal, Nano Lett. **9**, 427 (2009).
[5]D. Pantel, S. Goetze, D. Hesse, and M. Alexe, Nature Mater. **11**, 289 (2012).
[6]A. Chanthbouala, A. Crassous, V. Garcia, K. Bouzehouane, S. Fusil, X. Moya, J. Allibe, B. Dlubak, J. Grollier, S. Xavier, C. Deranlot, A. Moshar, R. Proksch, N. D. Mathur, M. Bibes, and A. Barthelemy, Nat. Nanotechnol. **7**, 101 (2011).
[7]C. Duan, F. S. Renat, N. M. Wei, S. J. Sitaram, and E. Y. Tsymbal, Nano Lett. **6**, 483 (2006).
[8]M. Hambe, A. Petraru, N. A. Pertsev, P. Munroe, V. Nagarajan, and H. Kohlstedt, Adv. Funct. Mater. **20**, 2436 (2010).
[9]M. Arredondo, Q. M. Ramasse, M. Weyland, R. Mahjoub, I. Vrejoiu, D. Hesse, N. D. Browning, M. Alexe, P. Munroe, and V. Nagarajan, Adv. Mater. **22**, 2430 (2010).
[10]L. Lymperakis, J. Neugebauer, M. Albrecht, T. Remmele, and H. P. Strunk, Phys. Rev. Lett. **93**, 196401 (2004).
[11]S. Y. Hu, Y. L. Li, and L. Q. Chen, J. Appl. Phys. **94**, 2542 (2003).
[12]Z. Zhang, W. Sigle, and M. Ruhle, Phys. Rev. B **66**, 094108 (2002).
[13]I. Vrejoiu, G. Le Rhun, L. Pintilie, D. Hesse, M. Alexe, and U. Gösele, Adv. Mater. **18**, 1657 (2006).
[14]L. Fitting, S. Thiel, A. Schmehl, J. Mannhart, and D. A. Muller, Ultramicroscopy **106**, 1053 (2006).
[15]M. Bosman, V. J. Keast, J. L. García-Muñoz, A. J. D'Alfonso, S. D. Findlay, and L. J. Allen, Phys. Rev. Lett. **99**, 086102 (2007).
[16]M. Bosman, K. Watanabe, D. T. L. Alexander, and V. J. Keast, Ultramicroscopy **106**, 1024 (2006).
[17]G. W. Pabst, L. W. Martin, Y.-H. Chu, and R. Ramesh, Appl. Phys. Lett. **90**, 072902 (2007).
[18]X. Qi, J. Dho, R. Tomov, M. G. Blamire, and J. L. MacManus-Driscoll, Appl. Phys. Lett. **86**, 062903 (2005).
[19]S. H. Lim, M. Murakami, W. L. Sarney, S. Q. Ren, A. Varatharajan, V. Nagarajan, S. Fujino, M. Wuttig, I. Takeuchi, and L. G. Salamanca-Riba, Adv. Funct. Mater. **17**, 2594 (2007).
[20]Y. H. Chu, T. Zhao, M. P. Cruz, Q. Zhan, P. L. Yang, L. W. Martin, M. Huijben, C. H. Yang, F. Zavaliche, H. Zheng, and R. Ramesh, Appl. Phys. Lett. **90**, 252906 (2007).
[21]G. Xu, H. Hiraka, G. Shirane, J. Li, J. Wang, and D. Viehland, Appl. Phys. Lett. **86**, 182905 (2005).
[22]M. P. de Jong, I. Bergenti, V. A. Dediu, M. Fahlman, M. Marsi, and C. Taliani, Phys. Rev. B **71**, 014434 (2005).
[23]H. Kurata and C. Colliex, Phys. Rev. B **48**, 2102 (1993).
[24]L. Samet, D. Imhoff, J. L. Maurice, J. P. Contour, A. Gloter, T. Manoubi, A. Fert, and C. Colliex, Eur. Phys. J. B **34**, 179 (2003).
[25]M. Bibes, L. Balcells, S. Valencia, J. Fontcuberta, M. Wojcik, E. Jedryka, and S. Nadolski, Phys. Rev. Lett. **87**, 067210 (2001).
[26]S. Estradé, J. Arbiol, F. Peiró, I. C. Infante, F. Sanchez, J. Fontcuberta, F. de la Peña, M. Walls, and C. Colliex, Appl. Phys. Lett. **93**, 112505 (2008).
[27]H. Dulli, P. A. Dowben, S. H. Liou, and E. W. Plummer, Phys. Rev. B **62**, R14629 (2000).
[28]J. L. Maurice, F. Pailloux, A. Barthélémy, O. Durand, D. Imhoff, R. Lyonnet, A. Rocher, and J. P. Contour, Philos. Mag. **83**, 3201 (2003).
[29]K. Han and K. Yu-Zhang, Philos. Mag. B **79**, 897 (1999).
[30]M. Fujimoto, J. Cryst. Growth **237–239**(Part 1), 430 (2002).
[31]S. H. Oh and C. G. Park, J. Appl. Phys. **95**, 4691 (2004).
[32]C. J. Lu, L. A. Bendersky, K. Chang, and I. Takeuchi, J. Appl. Phys. **93**, 512 (2003).
[33]A. E. Romanov, W. Pompe, S. Mathis, G. E. Beltz, and J. S. Speck, J. Appl. Phys. **85**, 182 (1999).